nature nanotechnology

LETTERS

https://doi.org/10.1038/s41565-020-0685-6

Check for updates

Odd- and even-denominator fractional quantum Hall states in monolayer WSe_2

Qianhui Shi[1], En-Min Shih[1], Martin V. Gustafsson[1,2], Daniel A. Rhodes[3], Bumho Kim[3], Kenji Watanabe[4], Takashi Taniguchi[4], Zlatko Papić[5], James Hone[3] and Cory R. Dean[1]✉

Monolayer semiconducting transition-metal dichalcogenides (TMDs) represent a unique class of two-dimensional (2D) electron systems. Their atomically thin structure facilitates gate tunability just like graphene does, but unlike graphene, TMDs have the advantage of a sizable band gap and strong spin–orbit coupling. Measurements under large magnetic fields have revealed an unusual Landau level (LL) structure[1–3], distinct from other 2D electron systems. However, owing to the limited sample quality and poor electrical contact, probing the lowest LLs has been challenging, and observation of electron correlations within the fractionally filled LL regime has not been possible. Here, through bulk electronic compressibility measurements, we investigate the LL structure of monolayer WSe_2 in the extreme quantum limit, and observe fractional quantum Hall states in the lowest three LLs. The odd-denominator fractional quantum Hall sequences demonstrate a systematic evolution with the LL orbital index, consistent with generic theoretical expectations. In addition, we observe an even-denominator state in the second LL that is expected to host non-Abelian statistics. Our results suggest that the 2D semiconductors can provide an experimental platform that closely resembles idealized theoretical models in the quantum Hall regime.

The fractional quantum Hall (FQH) effect results from strong Coulomb interactions driving a collective state within a partially filled LL[4]. The associated quasiparticle excitations are fractionally charged anyons with unconventional exchange statistics, providing one of the few opportunities to experimentally study an electronic system with fractional topological order. Despite more than three decades of efforts, several fundamental questions remain. While the FQH states in the lowest LL are relatively well understood, those in higher LLs are not; the $N=1$ LL (N is the LL orbital index), in particular, manifests delicate competition between FQH states and electronic solid states, and the FQH hierarchy exhibits parameter-dependent variations that do not follow a universal rule[5]. Additionally, an even-denominator state appears at half filling of the $N=1$ LL[6–10] that is presumed to host non-Abelian Majorana excitations[11–14]; however, the definitive experimental verification of these excitations is still lacking.

In conventional heterostructures such as GaAs and ZnO (refs. [4,6,7]), complications due to finite-thickness effects are always present. Moreover, the FQH states are generally fragile, with most states appearing only in the highest-mobility devices at sub-Kelvin temperatures. In monolayer (ML) graphene, by contrast, wide gate tunability and weak screening enable observation of the FQH states at an order of magnitude higher temperatures. However, the unique features of graphene also create new challenges. For example, the orbital wavefunction in the $N=1$ LL of ML graphene is an equal mixture of the non-relativistic $|0\rangle$ and $|1\rangle$ harmonic oscillator wavefunctions[15], which does not favour formation of the even-denominator states. Additionally, the four-fold degeneracy in ML graphene, due to the spin and valley degrees of freedom, further complicates the LL structure and may or may not modify the FQH spectrum, depending sensitively on the device details[16–18]. Finally, the lack of a robust band gap in graphene limits the ability to engineer electrostatically tunable mesoscopic structures, such as quantum point contacts and interferometers—important tools for unveiling the potentially exotic properties of various FQH states[19].

Semiconducting TMDs such as ML WSe_2 provide a potential opportunity to bridge the gap between conventional heterostructures and graphene. The spin and valley degrees of freedom are locked (see Fig. 1a)[20], which, together with an unusually large spin-splitting[3], yields a LL spectrum where the low energy levels are fully spin and valley polarized, effectively eliminating the degenerate degrees of freedom[3]. Although the $N=1$ LL orbital wavefunction in WSe_2 is formally also a mixture of $|0\rangle$ and $|1\rangle$ (refs. [21,22]) similar to graphene, the large band gap suppresses the weight of the $|0\rangle$ component to only a few percent, and the $|1\rangle$ component dominates[22].

Although the LL structure of semiconducting TMDs has been experimentally probed[1,3,23,24], observation of the FQH states has been elusive. This is largely due to a combination of limited material quality and poor electrical contact, both of which conspire to make the low density regime, where the FQH states may be observed, experimentally inaccessible[2,3]. Here we address both issues simultaneously by performing capacitance measurements on high-quality WSe_2. The samples were grown by a previously reported self-flux method, which yields a density of atomic defects below $10^{11}\,cm^{-2}$ (ref. [25]). The reduced sensitivity of the capacitance measurement to both large contact resistance and disorder-induced localization allows us to probe the electronic compressibility in the valence band all the way to the band edge.

Figure 1b shows a schematic of the device geometry and capacitance measurement scheme (see Methods and Supplementary Information Section 1 for device details including contact configuration). The capacitance measurement closely follows similar techniques that have been applied to both GaAs and graphene in the quantum Hall regime[9,18,26] (see Methods and Supplementary Fig. 2). In brief, we apply a small a.c. signal, V_{AC}, to one of the gates, and measure the induced a.c. voltage, V_P, on the other, while the ML WSe_2 is grounded. In the absence of dissipation, V_P is, to a good

[1]Department of Physics, Columbia University, New York, NY, USA. [2]Raytheon BBN Technologies, Cambridge, MA, USA. [3]Department of Mechanical Engineering, Columbia University, New York, NY, USA. [4]National Institute for Materials Science, Tsukuba, Japan. [5]School of Physics and Astronomy, University of Leeds, Leeds, UK. ✉e-mail: cd2478@columbia.edu

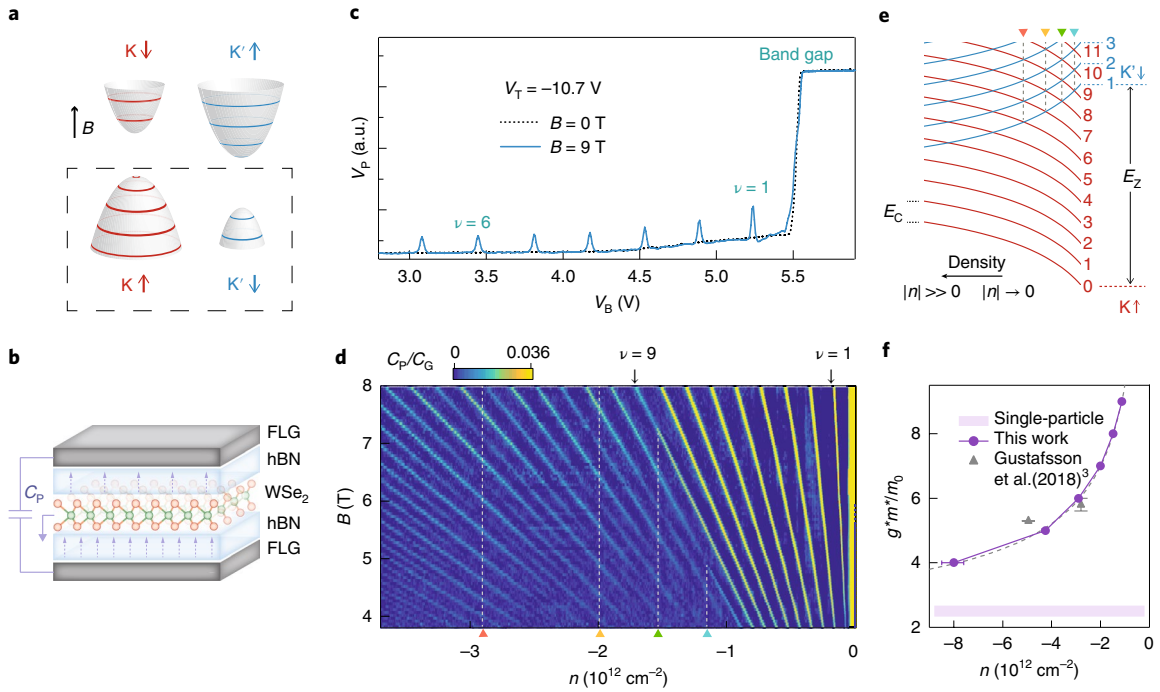

Fig. 1 | Measurement scheme and LL structure. a, Cartoon of the low-energy band structure subject to a perpendicular magnetic field. The dashed line box highlights the valence band, which is relevant in our study. **b**, Cartoon of the stack that illustrates the definition of penetration capacitance. ML WSe_2 flakes encapsulated between two hexagonal boron nitride (hBN) layers and few-layer graphite (FLG) flakes serve as top and bottom gates. **c**, Penetration signal as a function of the back gate voltage V_B at 0 T (dotted) and 9 T (solid), with top gate voltage $V_T = -10.7$ V. **d**, Penetration signal versus carrier density and the magnetic field measured at $T = 1.6$ K. The vertical dashed lines mark the densities where the contrast between strong and weak gaps is the most prominent. **e**, Schematic illustration of the evolution of a LL diagram as carrier density is varied. Red and blue curves stand for spin up and spin down branches, respectively, and the numbers on the right mark the LL orbital indices. The dashed lines illustrate the same densities as those in Fig. 1d, where level crossings (or anti-crossings) between LLs lead to the strongest variation of gaps at neighbouring integer filling factors. **f**, Magnetic susceptibility $\chi = E_Z/E_C = g^*m^*/m_0$ as a function of carrier density. The thick horizontal line marks the value from the bare g-factor and effective mass from a single-particle picture. The triangles mark the same quantity reported in the literature[3].

approximation, proportional to the penetration capacitance, C_P, which itself is proportional to the inverse bulk electronic compressibility, $n^2 d\mu/dn$, where n is carrier density and μ is the chemical potential of the WSe_2 (see Supplementary section 2). A small-valued V_P therefore indicates that the WSe_2 layer is compressible, whereas a large V_P indicates that it is incompressible, that is, gapped.

Figure 1c shows a plot of V_P versus back gate voltage V_B, measured at both zero and finite magnetic field at $T = 1.6$ K. At large V_B, the Fermi level of ML WSe_2 is in the band gap and the channel is insulating, yielding a plateau in V_P that corresponds to the maximum measurable penetration signal. Under zero magnetic field (dotted line), the signal drops sharply as V_B falls below 5.5 V, indicating that the Fermi level of ML WSe_2 enters the valence band. The channel is then compressible with a constant finite density of states, resulting in a small penetration signal. At $B = 9$ T (solid line), we observe the same general trend, but with multiple new peaks corresponding to the incompressible cyclotron gaps between the LLs. The peaks appear at integer filling factors $\nu = nh/eB$, where n is the hole carrier density determined from the geometric capacitance between the channel and the two gates, h is Planck's constant and e is the electron charge. Observation of a peak at all integer fillings indicates a fully lifted LL degeneracy.

In Fig. 1d we plot the penetration capacitance versus the magnetic field B and carrier density n at $T = 1.6$ K. The LL gaps demonstrate variations in the hierarchy as density is varied, switching between odd- and even-integer-dominated sequences. This is consistent with previous reports in TMDs[2,3], and results from level crossings (or anti-crossings) due to the exchange-enhanced and density-dependent spin-splitting energy between the two sets of LLs, $E_Z = 2g^*\mu_B B$ (g^* is the effective g-factor and $\mu_B = e\hbar/2m_0$ is the Bohr magneton, with ħ being the reduced Planck constant and m_0 the bare electron mass), as sketched in Fig. 1e. By tracking the density where the level crossings occur (see Supplementary Information Section 3), we determine the spin-susceptibility $\chi = E_Z/E_C = g^*m^*/m_0$ as a function of density (Fig. 1f), where E_C is the cyclotron energy and m^* is the effective mass of hole carriers. The capability to extend to the low density regime reveals that E_Z/E_C can be as large as nine, that is, 60% larger than previously identified and more than three times larger than the single-particle value, further attesting to the strong electron interaction effects in this system. Importantly, these results confirm a simple LL structure with fully lifted degeneracy for the lowest LLs—the regime where FQH states are expected—which we discuss below.

Now we focus on the lowest LLs under very large magnetic fields. In the top panel of Fig. 2a, the penetration signal V_P measured at $B = 29$ T and $T = 0.3$ K is plotted for filling factor range $0 < \nu < 3$. The top axis labels the corresponding orbital index for each filling range (see also Supplementary Information Sections 4 and 5). In addition to large V_P at integer ν, we observe peaks in V_P at fractional ν—which signals the chemical potential discontinuity due to the formation of FQH states—in all three LLs, including one at the seventh fractional filling in the $N = 2$ LL. For all states except $\nu = 1/3$ and 2/3, the phase due to the dissipative contribution shows a small and featureless response (Fig. 2a, bottom panel). The magnetic field dependence of the penetration capacitance is shown in Fig. 2b from $B = 11$ T to 29 T. The features that we have labelled evolve

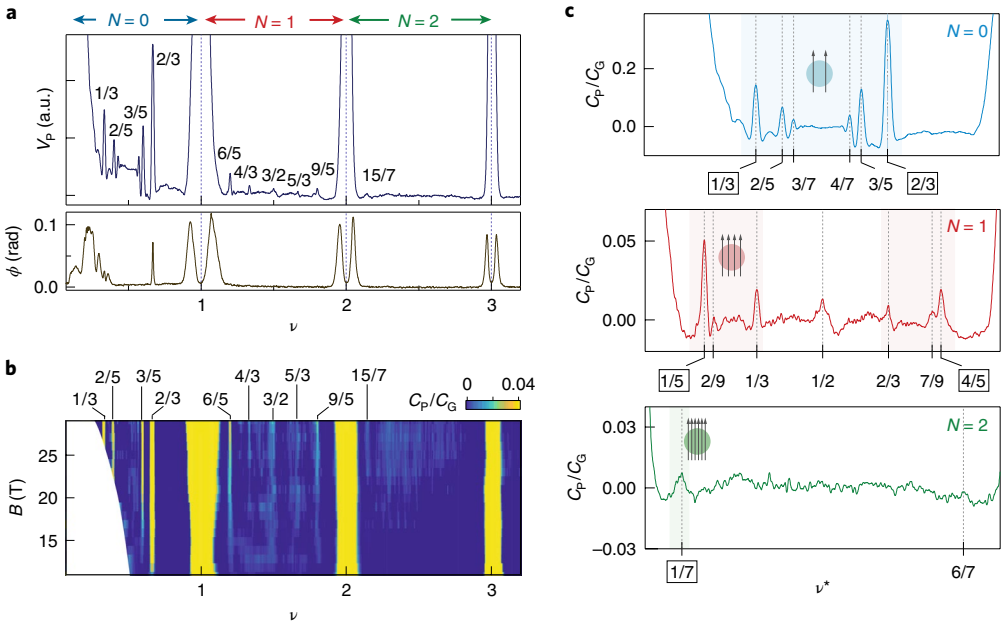

Fig. 2 | FQH states. a, Penetration signal (top) and the phase (bottom) versus filling factor ν. **b**, Penetration capacitance versus filling factor ν and magnetic field B. **c**, Penetration capacitance normalized by the geometry capacitance between the top and bottom gates, C_P/C_G, plotted versus the partial filling factor ν^*, for $N=0$ (top), $N=1$ (middle) and $N=2$ (bottom) at $B=29$ T and $T=0.3$ K. Filling factors where incompressible states appear are marked with vertical dotted lines, with the filling factor of the strongest states (and their conjugates) for each LL boxed. The inset cartoon illustrates the most prominent composite fermion construction for each LL, with the number of arrows illustrating the number of flux quanta attachment to each electron.

along vertical trajectories (that is, fixed filling fraction) and generally become better developed with increasing field, consistent with our interpretation that these represent the FQH states.

The FQH sequence shows a different hierarchy in each LL. We denote the fractional part of the filling factor as $\nu^* = \nu - N$ and plot the penetration capacitance normalized by the geometry capacitance, C_P/C_G, versus ν^*, for the three LLs with orbital index $N=0$, 1 and 2 in Fig. 2c. The state that manifests the largest variation in C_P (or its particle–hole conjugate at $1-\nu^*$) appears at $\nu^*=1/3$ in the $N=0$, 1/5 in the $N=1$ and 1/7 in the $N=2$ LL. This observation can be summarized by the simple rule that, in each LL, the most robust FQH state is at $\nu^*=1/(2N+3)$.

In addition to the strongest individual state in each LL, the overall sequence also shows a systematic trend. In the $N=0$ LL the FQH hierarchy follows the standard sequence that is observed in other 2D systems, with fractional states appearing at $\nu^*=n/(2n+1)$ where n takes integer values, and with the relative strength of each state diminishing with increasing n. This hierarchy is well described by the composite fermion (CF) model, in which strong electron–electron interactions are renormalized by attaching an even number of flux quanta to each electron (in this case, two flux per electron), resulting in weakly interacting CFs in reduced magnetic fields[27]. The two-flux FQH sequence, such as observed here, resembles an integer quantum Hall sequence but centred around the filling fraction $\nu=1/2$. In the $N=1$ LL, the FQH hierarchy changes. Here the $\nu^*=1/5$ and 4/5 states are the strongest, with smaller peaks also appearing at 2/9 and 7/9. This hierarchy is consistent with a four-flux sequence ($\nu^*=n/(4n+1)$) centred around 1/4 and 3/4 filling. Finally, for $N=2$, the only clearly resolved FQH state appears at $\nu=1/7$, which is the dominant fraction expected in a six-flux CF sequence ($\nu^*=n/(6n+1)$). This trend can also be summarized with a simple rule, namely, the most robust CF sequence observed in each LL corresponds to a CF $2p$-flux attachment series where $p=N+1$.

The systematic evolution of the FQH sequence with the LL orbital index results from the change of orbital wave funtion and interaction potential. Besides FQH states, strong interactions within a LL can drive competing ground states such as the electron solid phases[28,29]. The LL dependence that we observe is qualitatively consistent with a previously identified scaling argument[29] that considered this competition. In this view, FQH states are favoured when the inter-particle spacing, $d \sim l_B/\sqrt{\nu^*}$, is comparable to the interaction length scale, $R \sim 2R_C = 2\sqrt{2N+1}l_B$ (where R_C is the cyclotron radius and l_B is the magnetic length). The FQH states give way to a Wigner solid when $d>R$, or charge density wave states (stripe and bubble phases) when $d<R$. An example is illustrated schematically in Fig. 3a for the case of $\nu^*=1/5$, which according to this argument would favour a FQH ground state in the $N=1$ LL.

Figure 3b shows a schematic phase diagram summarizing the FQH states observed in our sample. Consistent with the scaling argument, odd-denominator states are observed within a band corresponding to $d\sim R$. Likewise, as the orbital index increases, the range of filling factors over which the FQH states are resolved decreases. We note that we do not identify unambiguous signatures of the solid phases. It is possible that the large response in the dissipative signal in Fig. 2b is due to the insulating Wigner crystal states, the boundaries of which move towards integer filling with increasing N.

The LL dependence we observe also shows excellent agreement with the exact diagonalization calculations of the quasiparticle–quasihole excitation energies. In Fig. 3c we plot the charge gap Δ (that is, the sum of energies required to create a single quasihole and a single quasielectron) for filling factors $\nu^*=1/3$, 1/5 and 1/7 as a function of N. The most robust FQH states for $N=0$, 1 and 2 are 1/3, 1/5 and 1/7, respectively, consistent with our experimental data. Figure 3c shows the gaps only for states that allow a reliable extrapolation to the thermodynamic limit, which coincide with the states that have a large overlap with the Laughlin wave function (see Supplementary Information Section 8).

Finally, we observe an even-denominator state at $\nu=3/2$, that is, half filling of the $N=1$ LL, as shown in the middle panel of

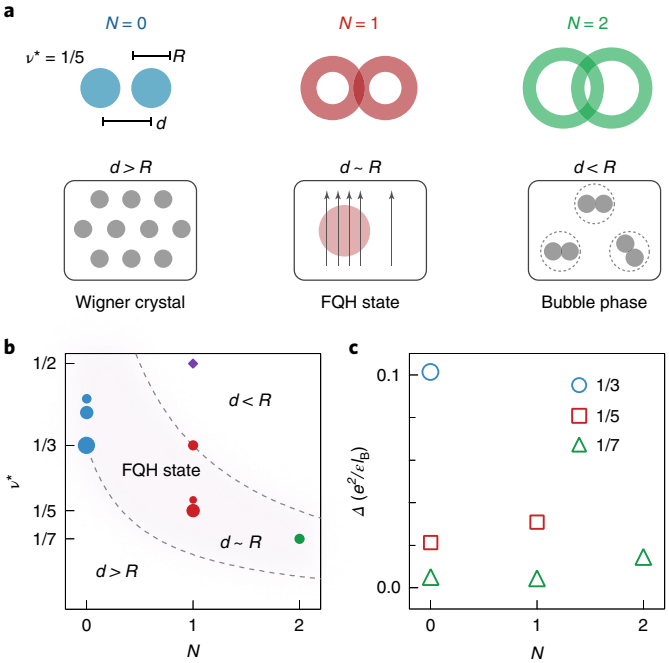

Fig. 3 | Evolution of FQH states with LL orbital index. a, Cartoon illustrating the evolution of the robustness of FQH states at different N for a fixed filling factor $\nu^*=1/5$. FQH states are the favourable ground states when the two length scales d and R are comparable. The discs and rings are drawn to qualitatively represent the wave functions in different LLs (in the symmetric gauge with angular momentum $m=0$). A ring shape is a good representation of the high-LL wave functions as the interaction potential assumes a plateau-like behaviour for $r<R$ (ref. [28]). **b**, Schematic phase diagram for FQH states. Odd- (even-)denominator states are marked by circles (diamonds). The area of the circle is proportional to the square root of the charge gap (integrated from $\partial\mu/\partial n$). The dashed lines are drawn at $R=\alpha d$ as suggested by the literature[28,29], and the factors α are chosen to bound the observed odd-denominator states. **c**, Numerically calculated charge gap for different filling fractions as a function of the LL index N.

Fig. 2c and as the diamond mark in Fig. 3b. The exclusive appearance of an even-denominator FQH state in the $N=1$ LL[6–10] is consistent with a Pfaffian[11], anti-Pfaffian[12,13] or particle–hole symmetric Pfaffian wave function[14], which is expected to host non-Abelian statistics (see Supplementary Information Section 9 for more discussion). Unlike other systems that have complications from multiple spin/valley degrees of freedom, making it difficult to disambiguate among other even-denominator candidate states such as the Halperin (331) state[18,30], the ML WSe_2 is isospin polarized and only one set of LLs is present at low carrier densities, so that the possibility of a two-component state can be ruled out. Single-component even-denominator FQH states have only been observed in a handful of high-mobility systems, including GaAs (refs. [6,31]), ZnO (ref. [7]) and graphene[8–10]. This makes our observation especially surprising since prior transport studies suggest that the WSe_2 mobility is limited to 30,000 $cm^2 V^{-1} s^{-1}$ (ref. [32]). One way the negative effect of disorder is addressed in our experiment is by applying large magnetic fields where the Coulomb interaction is maximized (at $B=29$ T, we observe a thermodynamic gap of about 1.6 K at $\nu=3/2$). We also note that the simple LL structure and wave functions in ML WSe_2 allow the even-denominator states to be strengthened at arbitrarily large magnetic fields, which was not possible in other systems due to concomitant complications such as the population of higher sub-bands in finite-thickness heterostructures or the severe modification of the orbital wave function in graphene[8–10]. Additionally, numerical calculations predict that a slight mixing of $|0\rangle$ in the $|1\rangle$ orbital wave functions, as is the case in the $N=1$ LL of WSe_2, optimizes the non-Abelian paired state[33,34].

While the overall FQH evolution we observe is consistent with theoretical expectations, previously studied systems showed different behaviours. For example, in most cases the 1/3 and 2/3 states remain the most prominent odd-denominator FQH states in the $N=1$ LL (that is, stronger than 1/5)[7,9,31], while the opposite behaviour is demonstrated in the two spin branches[5]. In the $N=2$ LL where we see the 1/7 state, the only FQH state previously reported in any system appeared at $\nu^*=1/5$ (refs. [35,36]). The deviation from theoretical models in previous systems is presumed to result from a variety of sample-specific properties such as finite-thickness effects[5,37], multi-component degrees of freedom[16–18] or more complex admixture wavefunctions[15]. The systematic evolution of the FQH hierarchy observed in ML WSe_2, by comparison, suggests that the semiconducting TMDs are a nearly ideal quantum Hall system in which experiments can be directly compared to simplified theoretical models (see Supplementary Information Section 6). The LL mixing parameter, characterized by the ratio between the Coulomb interaction energy scale and LL spacing, $\kappa=\frac{e^2}{\varepsilon l_B}/E_C \propto B^{-1/2}$ (where ε is the dielectric constant), is large in ML WSe_2: $\kappa\approx 7$ at $B=29$ T. Nevertheless, while LL mixing may be responsible for the particle–hole asymmetry in the FQH gap values in our sample, theoretical works have suggested that it does not substantially modify the FQH sequence[38] (see Supplementary Information Section 7).

To conclude, our compressibility measurements on ML WSe_2 reveal FQH states including those that have only been found in the highest-mobility systems. These observations attest to the advancement of the intrinsic quality of 2D semiconductors and establish them as a platform that is unique and sufficiently clean for further exploration of correlated electronic states.

Online content

Any methods, additional references, Nature Research reporting summaries, source data, extended data, supplementary information, acknowledgements, peer review information; details of author contributions and competing interests; and statements of data and code availability are available at https://doi.org/10.1038/s41565-020-0685-6.

Received: 21 November 2019; Accepted: 5 April 2020;
Published online: 6 July 2020

References

1. Wang, Z., Shan, J. & Mak, K. F. Valley- and spin-polarized Landau levels in monolayer WSe_2. *Nat. Nanotechnol.* **12**, 144–149 (2016).
2. Movva, H. C. P. et al. Density-dependent quantum Hall states and Zeeman splitting in monolayer and bilayer WSe_2. *Phys. Rev. Lett.* **118**, 247701 (2017).
3. Gustafsson, M. V. et al. Ambipolar Landau levels and strong band-selective carrier interactions in monolayer WSe_2. *Nat. Mater.* **17**, 411–415 (2018).
4. Tsui, D. C., Stormer, H. L. & Gossard, A. C. Two-dimensional magnetotransport in the extreme quantum limit. *Phys. Rev. Lett.* **48**, 1559 (1982).
5. Kleinbaum, E., Kumar, A., Pfeiffer, L. N., West, K. W. & Csáthy, G. A. Gap reversal at filling factors 3 + 1/3 and 3 + 1/5: towards novel topological order in the fractional quantum hall regime. *Phys. Rev. Lett.* **114**, 076801 (2015).
6. Willett, R. et al. Observation of an even-denominator quantum number in the fractional quantum Hall effect. *Phys. Rev. Lett.* **59**, 1776–1779 (1987).
7. Falson, J. et al. Even-denominator fractional quantum Hall physics in ZnO. *Nat. Phys.* **11**, 347–351 (2015).
8. Ki, D.-K., Fal'ko, V. I., Abanin, D. A. & Morpurgo, A. F. Observation of even denominator fractional quantum Hall effect in suspended bilayer graphene. *Nano Lett.* **14**, 2135–2139 (2014).
9. Zibrov, A. A. et al. Tunable interacting composite fermion phases in a half-filled bilayer-graphene Landau level. *Nature* **549**, 360–364 (2017).
10. Li, J. I. A. et al. Even-denominator fractional quantum Hall states in bilayer graphene. *Science* **358**, 648–652 (2017).
11. Moore, G. & Read, N. Nonabelions in the fractional quantum Hall effect. *Nuc. Phys. B* **360**, 362–396 (1991).

12. Levin, M., Halperin, B. I. & Rosenow, B. Particle-hole symmetry and the Pfaffian state. *Phys. Rev. Lett.* **99**, 236806 (2007).
13. Lee, S.-S., Ryu, S., Nayak, C. & Fisher, M. P. A. Particle-hole symmetry and the $\nu = \frac{5}{2}$ quantum Hall state. *Phys. Rev. Lett.* **99**, 236807 (2007).
14. Son, D. T. Is the composite fermion a dirac particle? *Phys. Rev. X* **5**, 031027 (2015).
15. Goerbig, M. O. Electronic properties of graphene in a strong magnetic field. *Rev. Mod. Phys.* **83**, 1193–1243 (2011).
16. Dean, C. R. et al. Multicomponent fractional quantum Hall effect in graphene. *Nat. Phys.* **7**, 693–696 (2011).
17. Feldman, B. E., Krauss, B., Smet, J. H. & Yacoby, A. Unconventional sequence of fractional quantum Hall states in suspended graphene. *Science* **337**, 1196–1199 (2012).
18. Zibrov, A. et al. Even-denominator fractional quantum Hall states at an isospin transition in monolayer graphene. *Nat. Phys.* **14**, 930–935 (2018).
19. de C. Chamon, C., Freed, D. E., Kivelson, S. A., Sondhi, S. L. & Wen, X. G. Two point-contact interferometer for quantum Hall systems. *Phys. Rev. B* **55**, 2331–2343 (1997).
20. Xiao, D., Liu, G.-B., Feng, W., Xu, X. & Yao, W. Coupled spin and valley physics in monolayers of MoS_2 and other group-VI dichalcogenides. *Phys. Rev. Lett.* **108**, 196802 (2012).
21. Li, X., Zhang, F. & Niu, Q. Unconventional quantum Hall effect and tunable spin Hall effect in Dirac materials: application to an isolated MoS_2 trilayer. *Phys. Rev. Lett.* **110**, 066803 (2013).
22. Rose, F., Goerbig, M. O. & Piéchon, F. Spin- and valley-dependent magneto-optical properties of MoS_2. *Phys. Rev. B* **88**, 125438 (2013).
23. Larentis, S. et al. Large effective mass and interaction-enhanced Zeeman splitting of K-valley electrons in $MoSe_2$. *Phys. Rev. B* **97**, 201407 (2018).
24. Pisoni, R. et al. Interactions and magnetotransport through spin-valley coupled Landau levels in monolayer MoS_2. *Phys. Rev. Lett.* **121**, 247701 (2018).
25. Edelberg, D. et al. Approaching the intrinsic limit in transition metal diselenides via point defect control. *Nano Lett.* **19**, 4371–4379 (2019).
26. Eisenstein, J. P., Pfeiffer, L. N. & West, K. W. Compressibility of the two-dimensional electron gas: measurements of the zero-field exchange energy and fractional quantum Hall gap. *Phys. Rev. B* **50**, 1760–1778 (1994).
27. Jain, J. K. *Composite Fermions* (Cambridge University Press, 2007).
28. Goerbig, M. O. & Smith, C. M. Scaling approach to the phase diagram of quantum Hall systems. *Europhys. Lett.* **63**, 736–742 (2003).
29. Goerbig, M. O., Lederer, P. & Smith, C. M. Competition between quantum-liquid and electron-solid phases in intermediate Landau levels. *Phys. Rev. B* **69**, 115327 (2004).
30. Halperin, B. I. Theory of the quantized Hall conductance. *Helv. Phys. Acta* **56**, 75–102 (1983).
31. Pan, W. et al. Exact quantization of the even-denominator fractional quantum Hall state at ν=5/2 Landau level filling factor. *Phys. Rev. Lett.* **83**, 3530–3533 (1999).
32. Pistunova, K. et al. Transport and photoluminescent characterization of high-quality single layer WSe_2 devices. In *APS March Meeting 2019* A15.007 (APS, 2019).
33. Apalkov, V. M. & Chakraborty, T. Stable Pfaffian state in bilayer graphene. *Phys. Rev. Lett.* **107**, 186803 (2011).
34. Papić, Z., Abanin, D. A., Barlas, Y. & Bhatt, R. N. Tunable interactions and phase transitions in Dirac materials in a magnetic field. *Phys. Rev. B* **84**, 241306 (2011).
35. Gervais, G. et al. Competition between a fractional quantum Hall liquid and bubble and Wigner crystal phases in the third Landau level. *Phys. Rev. Lett.* **93**, 266804 (2004).
36. Zeng, Y. et al. High-quality magnetotransport in graphene using the edge-free Corbino geometry. *Phys. Rev. Lett.* **122**, 137701 (2019).
37. Peterson, M. R., Jolicoeur, T. & das Sarma, S. Orbital Landau level dependence of the fractional quantum Hall effect in quasi-two-dimensional electron layers: finite-thickness effects. *Phys. Rev. B* **78**, 155308 (2008).
38. Sreejith, G. J., Zhang, Y. & Jain, J. K. Surprising robustness of particle-hole symmetry for composite-fermion liquids. *Phys. Rev. B* **96**, 125149 (2017).

Methods

Device fabrication. The device was built from exfoliated van der Waals materials using a dry transfer method in the following steps. First, hBN and graphite were picked up layer by layer and released on a silicon substrate, to serve as the bottom dielectric and gate. Second, Pt electrodes were evaporated onto the hBN and cleaned by an atomic force microscope tip in the contact mode. Third, hBN, graphite, hBN and ML WSe_2 were picked up layer by layer and released onto the bottom hBN with pre-patterned Pt electrodes. All transfer was assisted by polypropylene carbonate on polydimethylsiloxane on a glass slide, with the picking-up temperature about 40 °C and the releasing temperature about 120 °C. Finally, the top graphite was etched to define the top gate so that the cross-section between the top and bottom gates uniformly covered the ML WSe_2. Figure 1 in the Supplementary Information shows the optical micrograph image of the device.

Measurements. The carrier density in ML WSe_2 is controlled by d.c. gate voltages V_T and V_B, and $n=(C_tV_T+C_bV_B)/e$ where C_t (C_b) is the geometry capacitance between WSe_2 and the top (bottom) gate. The top gate is held at a constant high negative voltage in order to tune the WSe_2 in contact with Pt to a high density, allowing sufficient electrical contact to charge the WSe_2 flake, and the bottom gate is swept to tune the density. For our ML WSe_2, the measured capacitance does not appear to show any dependence on the displacement field $D\propto C_tV_T-C_bV_B$. An a.c. excitation δV_{ex} is superposed on V_B, and the penetration signal is detected from the top gate with the help of a FHX35X high electron mobility transistor (HEMT). The HEMT is biased with a d.c. current I_H and its working point is set by the gate voltage V_H, both controlled independently from V_T and V_B. The a.c. voltage drop across the HEMT δV_{out} is measured using lock-in amplifiers. The data presented are measured at 13.353 kHz using a 4 mV excitation. The capacitance measurement scheme is illustrated in Supplementary Fig. 2.

Data availability

The data that support the plots within this paper and other findings of this study are available at https://doi.org/10.5518/807.

Acknowledgements

We thank M. Goerbig, A. Kormanyos and F. Zhang for discussion, and W. Coniglio and B. Pullum for help with experiments. This research is primarily supported by the US Department of Energy (DE-SC0016703). Synthesis of WSe_2 (D.R. and B.K.) was supported by the Center for Precision Assembly of Superstratic and Superatomic Solids, a Materials Science and Engineering Research Center (MRSEC), through NSF grant DMR-1420634. A portion of this work was performed at the National High Magnetic Field Laboratory, which is supported by National Science Foundation Cooperative Agreement no. DMR-1157490 and the state of Florida. Z.P. acknowledges support by EPSRC grant EP/R020612/1. K.W. and T.T. acknowledge support from the Elemental Strategy Initiative conducted by the MEXT, Japan and the CREST (JPMJCR15F3), JST.

Author contributions

Q.S. fabricated the device with the help of E.S.; M.V.G. contributed to the development of the measurement set-up. Q.S. performed the measurements and analysed the data. Z.P. performed the numerical calculations. D.A.R. and B.K. grew the WSe_2 crystals. K.W. and T.T. grew the hBN crystals. J.H. and C.R.D. advised on the experiments. The manuscript was written with input from all authors.

Competing interests

The authors declare no competing interests.

Additional information

Supplementary information is available for this paper at https://doi.org/10.1038/s41565-020-0685-6.

Correspondence and requests for materials should be addressed to C.R.D.

Peer review information *Nature Nanotechnology* thanks Jinfeng Jia and the other, anonymous, reviewers for their contribution to the peer review of this work.